Phase-Pure Hybrid Layered Lead Iodide Perovskite Films Based on a Two-Step Melt-Processing Approach

Tianyang Li,[†] Andrew M. Zeidell,[§] Gamze Findik,[∥] Wiley A. Dunlap-Shohl,[†] Julie Euvrard,[†] Kenan Gundogdu,[∥] Oana D. Jurchescu,[§] and David B. Mitzi*[†,‡]

[†]Department of Mechanical Engineering and Materials Science and [‡]Department of Chemistry, Duke University, Durham, North Carolina 27708, United States

[§]Department of Physics and Center for Functional Materials, Wake Forest University, Winston-Salem, North Carolina 27109, United States

[∥]Department of Physics, North Carolina State University, Raleigh, North Carolina 27606, United States

Ⓢ *Supporting Information*

ABSTRACT: Layered lead halide perovskites have recently been heavily investigated due to their versatile structures, tunable electronic properties, and better stability compared with 3D perovskites and have also been effectively incorporated into photovoltaic and light-emitting devices. They are often prepared into thin film form by solution methods and typically contain a mixture of phases with different inorganic layer thicknesses (denoted by "n"). In addition, melt-processing has recently been introduced as an option for film deposition of $n = 1$ lead iodide-based perovskites. Here, we study the thermal

properties of higher n ($n > 1$) layered perovskites in the family (β-Me-PEA)$_2$MA$_{n-1}$Pb$_n$I$_{3n+1}$, with $n = 1$, 2, and 3 and where β-Me-PEA = β-methylphenethylammonium and MA = methylammonium, and reveal that they do not melt congruently. However, they can still be melt-processed in air by using a two-step process that includes a lower temperature postannealing step after the initial brief melting step. While typically higher n films contain a mixture of the different n phases, the resulting two-step melt-processed films are highly crystalline and phase pure. Optical and electrical properties of these films were further characterized by time-resolved photoluminescence and dark/illuminated transport measurements, showing the same order of magnitude single-exciton recombination rates compared to previous single crystal results and >2 orders of magnitude higher conductivity compared to conventional spin-coated films. These results offer new pathways to study the layered perovskites and to integrate them into electronic and optoelectronic devices.
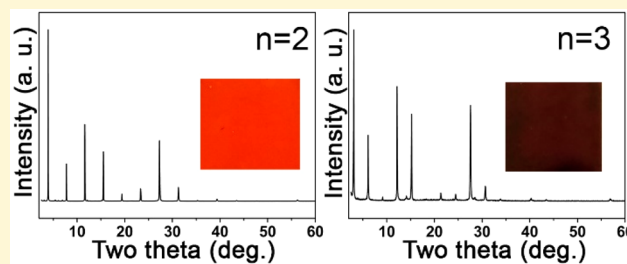
INTRODUCTION

Hybrid organic−inorganic perovskite materials, especially lead halide-based hybrid perovskites, have attracted considerable research interest over the past few years due to their unique optoelectronic properties, and the performance of the photovoltaic and light-emitting devices based on these materials has rapidly improved.[1−12] Among these materials, two-dimensional layered perovskite phases (with a general formula of (RNH$_3$)$_2$MA$_{n-1}$Pb$_n$I$_{3n+1}$, known as Ruddlesden−Popper phases) show greater structural diversity and environmental stability and have been widely studied since the 1990s.[13−15] Optoelectronic properties (e.g., band gap energy) of these layered systems can be tuned by altering the inorganic layer thickness (i.e., "n"), and they have been proven as promising active layers in solar cells and light-emitting diodes with high efficiencies.[10,16−20]

For device integration, thin films of these materials are typically prepared by solution-based processes due to the low cost associated with these methods, most commonly spin-coating, which allows for the formation of crystalline films of tunable thickness at low annealing temperatures.[21−25] Post-processing methods such as solvent annealing are often used to improve film morphology and optoelectronic properties.[26] One disadvantage of these processes is that, when preparing perovskite films with $n \geq 2$, a mixture of layered perovskite phases with various n (including the 3D perovskite MAPbI$_3$) is generally observed within the film.[13,17,27,28] This can greatly obscure the characterization of the films and bring ambiguity to the analysis of the properties of layered phases with a particular n number.

As an alternative to solution processing, melt-processing has proven successful for polymers and inorganic materials, as well as hybrid materials. It allows for the possibility of high throughput roll-to-roll, lamination, capillary filling, and extrusion methods.[29−36] Previously, we demonstrated that with careful structural modification the thermal properties of

hybrid layered $n = 1$ tin and lead halide perovskites can be tuned, and high quality films can be fabricated by using a melt-processing approach.[29,30,37,38] Design rules have also been established for targeting layered perovskites with low melting temperature; e.g., modifying the organic cation to introduce steric hindrance near the ammonium tethering group generally leads to lower melting temperature.[29,30,37,38] However, those $n = 1$ lead iodide perovskites that do melt have a relatively large band gap energy (~2.5 eV), rendering them less attractive for many optoelectronic applications. In this respect, making phase-pure, smaller-band gap $n > 1$ films is of particular interest for device applications and also for characterization of intrinsic properties.

Here we show that using β-methylphenethylammonium (β-Me-PEA) and methylammonium (MA) as the organic cations, layered lead iodide perovskites with $n = 1$, 2, and 3 (i.e., (β-Me-PEA)$_2$PbI$_4$, (β-Me-PEA)$_2$MAPb$_2$I$_7$, and (β-Me-PEA)$_2$MA$_2$Pb$_3$I$_{10}$, respectively) can be made. Compared to the $n = 1$ compound, the perovskites with $n = 2$ and 3 melt incongruently at higher temperatures. Nevertheless, highly crystalline and phase pure films can still be prepared by using a modified melt-processing approach involving the addition of controlled amounts of extra organic iodide salts and a moderate postannealing treatment.

■ EXPERIMENTAL SECTION

Chemicals. β-Methylphenethylamine (β-Me-PEA, 99%, Sigma-Aldrich), methylammonium iodide (MAI, 99%, Greatcell), lead iodide (PbI$_2$, 99.99%, TCI Chemicals), and hydriodic acid (HI) solution (57 wt %, stabilized, 99.95%, Sigma-Aldrich) were used without further purification.

Synthesis Details. *(β-Me-PEA)$_2$PbI$_4$ (n = 1).* Stoichiometric amounts of PbI$_2$ (0.25 mmol) and β-Me-PEA (0.5 mmol) were added into a 3 mL HI solution. The solution was then heated to 100 °C to dissolve all solids and then slowly cooled at 2 °C/h to room temperature. The orange crystals were collected by filtration and then washed with diethyl ether repeatedly. Yield: 40.2%.

(β-Me-PEA)$_2$MAPb$_2$I$_7$ (n = 2). PbI$_2$ (1 mmol), MAI (0.5 mmol), and β-Me-PEA (0.25 mmol) were added into a 1.5 mL HI solution. The solution was then heated to 100 °C to dissolve all solids and then slowly cooled at 2 °C/h rate to room temperature. The red crystals were collected by filtration and then washed with diethyl ether repeatedly. Yield: 9.2% (based on Pb).

(β-Me-PEA)$_2$MA$_2$Pb$_3$I$_{10}$ (n = 3). PbI$_2$ (1 mmol), MAI (0.667 mmol), and β-Me-PEA (0.065 mmol) were added into a 1.5 mL HI solution. The solution was then heated to 100 °C to dissolve all solids and then slowly cooled at 2 °C/h rate to room temperature. The deep brown crystals were collected by filtration and then washed with diethyl ether repeatedly. Yield: 5.5% (based on Pb).

Melt-Processed Film Preparation. For the $n = 1$ layered perovskite films, β-Me-PEA$_2$PbI$_4$ powder was mixed with 5 wt % corresponding organic ammonium iodide salt (β-Me-PEAI). 0.5 mg of the powder was placed onto a 1.2 mm thick glass substrate and then covered with a piece of 8 μm thick Kapton sheet. The substrate was placed onto a preheated hot plate (temperature set to 215 °C) and pressed on top with another preheated glass substrate. After the solid melted and formed a yellow liquid, the substrate was then removed from the hot plate and cooled naturally. Processing was done under ambient conditions (i.e., in air).

For the $n = 2$ layered perovskite film, a film was first deposited on a glass substrate by drop-casting or doctor-blading from a 0.02 M (with respect to Pb^{2+}) THF solution or spin-coating (3000 rpm, 30 s in the glovebox) from a 0.2 M (with respect to Pb^{2+}) DMF solution of the $n = 2$ compound mixed with an additional 3 wt % of MAI and 6 wt % of β-Me-PEAI. The film was then melt-processed at 255 °C for 30 s under a Kapton or glass cover, followed by 30 min postanneal at 150 °C. For achieving single-phase $n = 2$ films, the postanneal time must

increase with increasing film thickness, which may be controlled by the concentration of the initial precursor solution or the RPM during spin-coating. Typically, the above-described process will lead to an ~250 nm thick film, and doubling the precursor concentration will lead to doubling the film thickness. Processing was done under ambient conditions (i.e., in air).

For the $n = 3$ layered perovskite film, a film was first deposited on a glass substrate by drop-casting or doctor-blading from a 0.02 M (with respect to Pb^{2+}) THF solution or spin-coating (3000 rpm, 30 s in the glovebox) from a 0.2 M (with respect to Pb^{2+}) DMF solution of the $n = 3$ compound mixed with an additional 6 wt % of MAI and 3 wt % of β-Me-PEAI. The film was then melt-processed at 255 °C for 30 s under a Kapton or glass cover, followed by 30 min of postanneal at 150 °C. For achieving single-phase $n = 3$ films, the postanneal time must increase with increasing film thickness, which may be controlled by the concentration of the initial precursor solution or the RPM during spin-coating. Typically, the above-mentioned process will lead to an ~250 nm thick film, and doubling the precursor concentration will double the film thickness. Processing was done under ambient conditions (i.e., in air).

Characterization Methods. Thermogravimetric analysis (TGA) measurements were performed on a TA Q50 instrument using a 5 °C/min ramping rate from 25 to 400 °C under nitrogen gas flow and with a 2 mg sample size. Differential scanning calorimetry (DSC) measurements were performed using a TA Discovery DSC instrument at a ramping rate of 5 °C/min from 25 to 300 °C using a hermetically sealed aluminum pan and lid with a 1 mg sample loading.

X-ray diffraction (XRD) measurements were performed on a PANalytical Empyrean Powder X-ray diffractometer using Cu Kα radiation, with the X-ray tube operating level at 45 kV and 40 mA. Temperature-dependent *in situ* XRD measurements were performed on a PANalytical Empyrean Powder X-ray diffractometer equipped with an XRK 900 reactor chamber using Cu Kα radiation. The sample powder was loaded onto a ceramic holder and scanned from 3° to 30° 2θ repeatedly (each scan takes 2 min) and ramped from room temperature to 255 °C continuously at 10 °C/min under a nitrogen atmosphere and then cooled to room temperature at 20 °C/min.

Morphologies of the spin-coated and melt-processed films were imaged with a scanning electron microscope (SEM, FEI XL30 SEM-FEG or Hitachi S-4700 field-emission SEM). The thickness of the films was estimated based on cross-sectional SEM images.

Optical absorption measurements were performed on a Shimadzu UV-3600 spectrophotometer. Photoluminescence (PL) measurements were performed on a Horiba Jobin Yvon LabRam ARAMIS system using a 442 nm Kimmon Koha He−Cd laser as excitation.

Time-resolved PL experiments were accomplished utilizing a commercial time-correlated single photon counting (TCSPC) spectrometer by Edinburgh Instruments (LifeSpec II). A Hamamatsu R3809U-50 photomultiplier tube housed in a Peltier cooler is used to detect PL. 100 fs pulses at 800 nm from a Ti:sapphire oscillator (Chameleon Ultra II from Coherent) are used as the optical source. The pulses are picked at 4 MHz repetition rate (Coherent 9200 Pulse Picker) and then converted to 400 nm using an APE-GmbH SHG unit. PL dynamics are modeled by the differential rate equation

$$\frac{d[N(t)]}{dt} = -k_1 N(t) - k_2 N^2(t) \tag{1}$$

where N is the photogenerated charge density and t is the delay time. k_1 and k_2 denote the monomolecular and bimolecular recombination rate constants, respectively. Because the excited-state populations of our samples are primarily composed of excitons, we can assign the first term in our model equation to single exciton recombination and the second to exciton−exciton annihilation.

The solution of eq 1 is

$$N(t) = \frac{N_0 k_1}{(k_1 + k_2 N_0) \exp(k_1 t) - k_2 N_0} \tag{2}$$

where N_0 is the carrier density at $t = 0$. Because $N(t)$ is proportional to the PL counts, the normalized intensity is proportional to $N(t)/N_0$:

$$\frac{I(t)}{I(0)} \propto \frac{N(t)}{N_0} = \frac{k_1}{(k_1 + k_2 N_0)\exp(k_1 t) - k_2 N_0} \qquad (3)$$

By fitting our normalized data to the above equation, we extracted the exciton recombination decay constant k_1 for our samples. The bimolecular recombination rate constants k_2 cannot be obtained directly. The constant fitting yields the $(k_2 \times N_0)$ combination of the decay constant k_2 and the initial density of excited carriers N_0, and we report this value instead.

Two-point transport measurements were conducted in a nitrogen atmosphere using an Agilent 4155C semiconductor parameter analyzer, considering various channel widths from 200 to 1000 μm (with 200 μm increment) and lengths from 30 to 100 μm (with 10 μm increment). Electrodes were deposited thermally using an Angstrom EvoVac evaporator operating at a base pressure of 2×10^{-6} Torr, with 80 nm of Au first, followed by 500 nm of Ag. The initial deposition rate of Au was set to 0.1 Å/s for the first 5 Å and then 0.2 Å/s for the next 5 Å, followed by 1 Å/s for the rest of the deposition. A 0.8 mW broadband fiber-coupled LED was used as the light source (Thorlabs, MBB1F1). For transient photo-I−V measurements, the intensity of the LED was held at 233 mW/m^2. The LED was cycled on and off with a period of 2.5 s, and photo-I−V measurements were taken while holding the voltage at 1, 2, 5, and 10 V.

The responsivity of the film is calculated via the equation

$$R = \frac{J_{ph}}{L_{light}} = \frac{J_{illuminated} - J_{dark}}{L_{light}} \qquad (4)$$

where J_{ph} (mA/cm^2) is the photocurrent density and L_{light} (μW/cm^2) is the incident light intensity.

■ RESULTS AND DISCUSSION

As reported previously, the melting transition temperatures of phenethylammonium (PEA)-based $n = 1$ layered lead iodide perovskites can be effectively tuned by introducing substituents at different positions on the PEA molecule. With a methyl group at the β position, the resulting compound has the lowest melting temperature (among the variants considered) at ∼207 °C, below the decomposition point and enabling high quality melt-processed films to be prepared in air.[37] A similar strategy was adopted here to target melt-processing in higher n compounds. First, compounds with $n = 2$ and 3 were synthesized and studied by using powder X-ray diffraction (XRD), thermogravimetric analysis (TGA), and differential scanning calorimetry (DSC). XRD patterns of as-made $n = 1$, 2, and 3 ground crystals (Figure 1a) show a series of peaks from $(00l)$ reflections due to the 2D nature of these compounds. These powder diffraction patterns resemble those of previously reported Ruddlesden−Popper perovskites with butylammonium as the large organic cation.[13] Because the exact crystal structures of these compounds are not yet determined, profile fittings were attempted using triclinic unit cells similar to those of the closely related phenethylamine-based layered compounds (Figures S1−S3). The interlayer distances extracted from the fitting results are 16.53, 22.85, and 29.20 Å for $n = 1$, 2, and 3 compounds, respectively, with the difference between successive n matching the thickness of one lead iodide corner-sharing layer (∼6.3 Å). The TGA and DSC curves (Figure 1b,c) suggest that these higher n phases are stable up to 200 °C, like for the $n = 1$ compound, with at least one structural transition below this point. Multiple transitions are observed from the DSC scans, and compared to the $n = 1$ compound, the melting transition temperatures (in this case, signifying incongruent melting into liquid melt and MAPbI$_3$) move up considerably to 248.6 and 248.2 °C, respectively, for

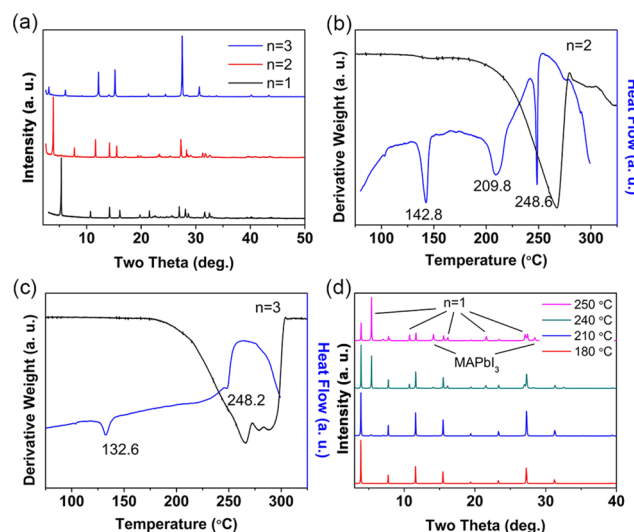**Figure 1.** (a) Powder XRD patterns of $n = 1$, 2, and 3 layered perovskite compounds. (b, c) TGA and DSC scans of $n = 2$ (β-Me-PEA)$_2$MAPb$_2$I$_7$ and $n = 3$ (β-Me-PEA)$_2$MA$_2$Pb$_3$I$_{10}$ perovskites. (d) *Ex situ* XRD experiment of $n = 2$ (β-Me-PEA)$_2$MAPb$_2$I$_7$ layered perovskite powder annealed at the specified temperatures for 30 s.

$n = 2$ and 3 compounds. The melting behavior is also visually confirmed by heating the powder samples under a glass cover above the melting point on a hot plate.

An *ex situ* experiment involving annealing the powder samples on the hot plate indicates that the $n = 2$ and 3 layered compounds do not melt congruently; i.e., they will not completely transform into the liquid form but become a liquid/solid mixture. As an example, the $n = 2$ perovskite powder was annealed (under a Kapton sheet cover) at different temperatures (Figure 1d) and then cooled naturally. The crystallinity of the sample improves upon annealing below 200 °C, as evidenced by the narrowing of the peak width. Above 210 °C, where the first phase transition occurs based on the DSC data, phase segregation results in a mixture of $n = 1$, 2 and the 3D MAPbI$_3$. When (partially) melted above 250 °C and resolidified upon cooling, it is obvious that the $n = 1$ phase is one of the major components of the resulting mixture. From these results, we hypothesize that above 210 °C the $n = 2$ compound undergoes a first step of incongruent melting wherein the $n = 1$ phase partially comes out of the structure and melts. However, this step cannot be clearly visualized (unlike the transition at 248.6 °C) due to the small amount of $n = 1$ melt liquid. A second stage of incongruent melting occurs at 248.6 °C, resulting in a definitive melt liquid and MAPbI$_3$.

We further performed an *in situ* temperature-dependent XRD experiment to carefully study the transition details during heating and cooling and to confirm the incongruent melting behavior. A structural phase transition (marked by the orange box) was detected for the $n = 2$ compound at ∼140 °C, as evidenced by the sudden peak shift (Figure 2a), agreeing with the results from the DSC study. This higher temperature structure is yet to be determined. Another transition (marked by the red box) was observed above 200 °C (again agreeing with DSC results), with the slow decrease of the first peak at $2\Theta = \sim4°$ and emergence of a new peak at $2\Theta = \sim6°$. Like the *ex situ* experiment, we attribute this transition to the phase segregation of the $n = 1$ phase, leading to the destruction of the original $n = 2$ structure. The $n = 1$ compound melts at this elevated temperature; therefore, it is not directly seen in the
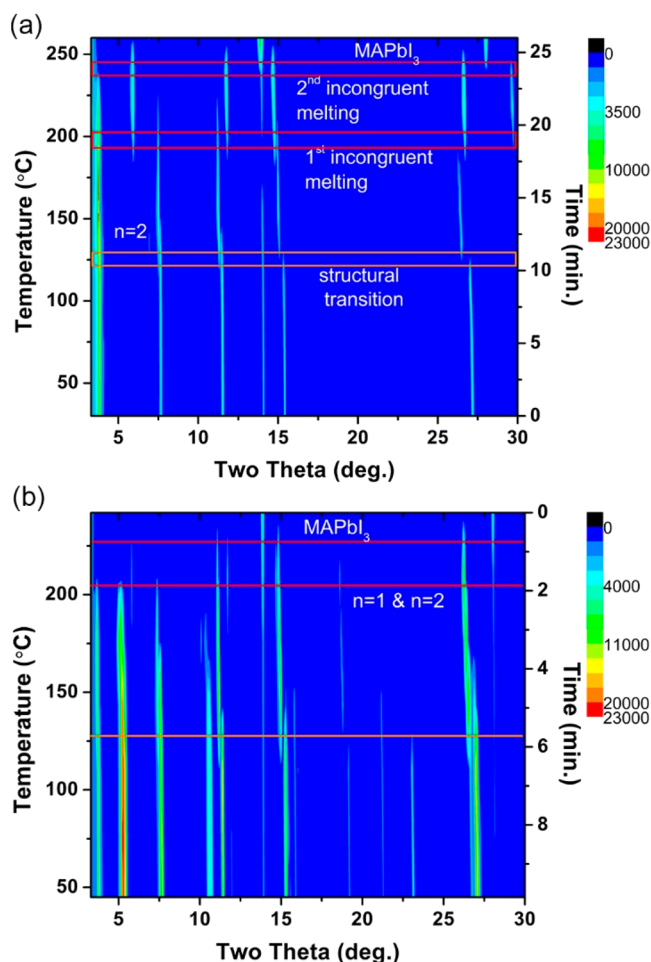
Figure 2. *In situ* temperature-dependent XRD measurement of $n = 2$ (β-Me-PEA)$_2$MAPb$_2$I$_7$ layered perovskite during (a) heating (10 °C/min) and (b) cooling (−20 °C/min).

XRD pattern, and the remaining peaks belong to an unknown intermediate phase that may also be organic deficient (compared to the original $n = 2$ phase). Before 250 °C there is another melting transition (marked by the red box). No peaks from the layered perovskites can be observed above 250 °C and these structures must therefore have gone into the melt phase; however, the 3D phase MAPbI$_3$ still remains as a solid[39] and is detected by the XRD scan at this temperature (i.e., note the (110) and (220) reflections of MAPbI$_3$ at $2\Theta = {\sim}14°$ and 28°). This result supports the hypothesis of incongruent melting behavior of the high n layered perovskites. We subsequently performed a cooling scan (Figure 2b), mimicking the procedures of melt-processing on the hot plate. Upon cooling, similar transitions (marked by the red and orange lines) happen in reverse order and can be clearly identified. The $n = 1$ and 2 phases solidify below 200 °C, showing predominately (00l) reflections of these phases. This leads to a mixture of $n = 1$, 2 and MAPbI$_3$ at room temperature, similar to what is observed in the *ex situ* experiment. The assignment of peaks of these phases in the pattern can be found in Figure S4.

Because of the incongruent melting behavior, it is increasingly difficult to make continuous homogeneous $n > 1$ films via a traditional, single-step melt-processing approach using solid powder (as we did for $n = 1$ compounds[36]). Therefore, the procedure was modified to involve depositing

the initial perovskite film by either drop-casting, doctor-blading, or spin-coating and then subjecting the resulting deposit to a thermal treatment at higher temperature (i.e., the melt-processing step) to get highly crystalline and phase-pure films. To mitigate the loss of organics during the annealing, appropriate amounts of extra organic iodide salts methylammonium iodide (MAI) and β-methylphenethylammonium iodide (β-Me-PEAI) were added into the precursor solution (see Experimental Section for details). The phase purity of the product film after melt-processing heavily depends upon the percentage of both extra salts added. The amount added is optimized through a trial-and-error process based on the specific annealing temperature and time sequence. Typically, decreasing the amount of MAI or increasing the amount of β-Me-PEAI from the optimal percentage range will lead to inclusion of lower n phase impurities in the final film, while increasing MAI or decreasing β-Me-PEAI will lead to higher n phase impurities. By use of a thin Kapton sheet (8 μm thick) or a glass slide as cover, $n = 1$ layered perovskite films were made under ambient conditions (i.e., in air) following the previously reported method.[36] For $n = 2$ and 3, a high-temperature melting step was first applied for 30 s, followed by a low-temperature (150 °C) postanneal step. Both steps were performed under a Kapton or glass cover. The optimal postanneal time varied from 30 to 120 min, depending on the film thickness. The introduction of the postannealing step facilitates ion movement and induces the reaction between the phase mixture. As a result, the initial phase segregation from incongruent melting can be healed, and phase pure films are obtained.

Figure 3 shows the XRD patterns and the optical characterization results of the melt-processed films of $n = 1$, 2, and 3 layered perovskites. For each of the three films, the XRD pattern is dominated by only one set of narrow (00l) reflection peaks, suggesting good crystallinity and strong preferred orientation parallel to the substrate. The peak positions also closely match those from the powder XRD pattern of the corresponding layered perovskites (see Figure 1a); i.e., no obvious phase segregation can be detected by typical diffraction-based characterization methods. (Only a trace amount of impurity can be seen from a more sensitive square-root intensity scale plot in Figure S5; however, these trace impurities cannot be detected by other characterization methods like absorption or photoluminescence.) The $n = 1$ film appears to be yellow, $n = 2$ bright red, and $n = 3$ brown (Figure 3, inset), similar to the colors of their single crystal counterparts. The film colors also agree with the absorption spectra (Figure 3b,d,f). In the spectra, no peak or absorption onset is observed before the corresponding excitonic absorption peak of the appropriate $n = 1$, 2, and 3 perovskites; in contrast, spin-coated films often exhibit an onset at ${\sim}700$ nm, indicative of 3D perovskite inclusion. The band gap energies of $n = 1$, 2, and 3 layered perovskite films are estimated to be approximately 2.4, 2.2, and 2.0 eV (calculated from the peak maxima of the excitonic absorption peaks), also very close to reported values determined for phase pure single crystals of similar (different large organic cation) $n = 1$, 2, and 3 samples.[13,40]

It is well-known that "energy funneling"[10] occurs in spin-coated layered perovskite films, which contain mixtures of phases with different n number. As a result, the PL peak red-shifts compared to a phase-pure crystal of a targeted n number, often occurring at ${\sim}700$ nm for $n > 2$ compositions. The
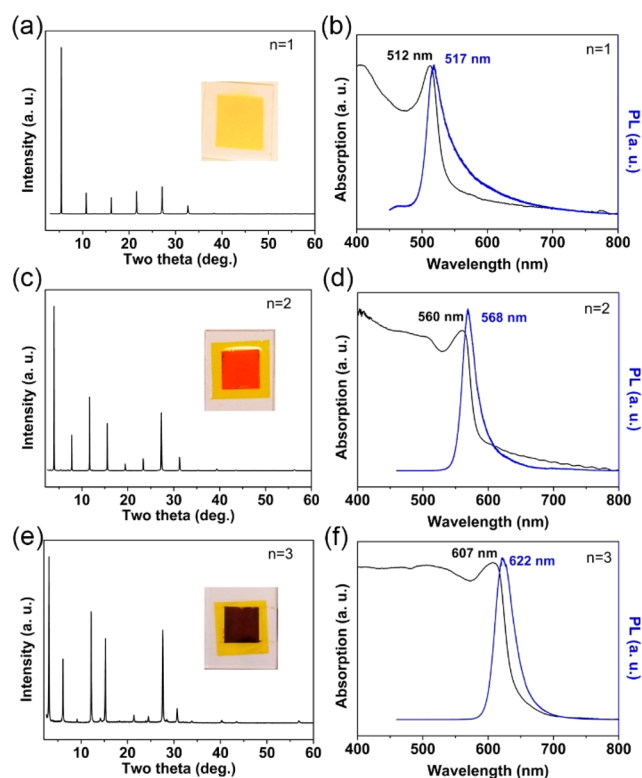
Figure 3. XRD patterns, UV−vis absorption, and photoluminescence spectra of (a, b) $n = 1$ (β-Me-PEA)$_2$PbI$_4$, (c, d) $n = 2$ (β-Me-PEA)$_2$MAPb$_2$I$_7$, and (e, f) $n = 3$ (β-Me-PEA)$_2$MA$_2$Pb$_3$I$_{10}$ layered perovskite melt-processed films. Inset: pictures of $n = 1$, 2, and 3 melt-processed films under a Kapton cover.

within a reasonable amount of time, possibly due to slower ion migration at that temperature.

Good phase purity of the melt-processed films offers the opportunity to characterize the intrinsic properties of the corresponding layered perovskites in thin film form. In this regard, we performed time-resolved photoluminescence (TRPL) measurements on $n = 1$, 2, and 3 melt-processed films (Figure 4a−c). The PL decay is modeled by a differential
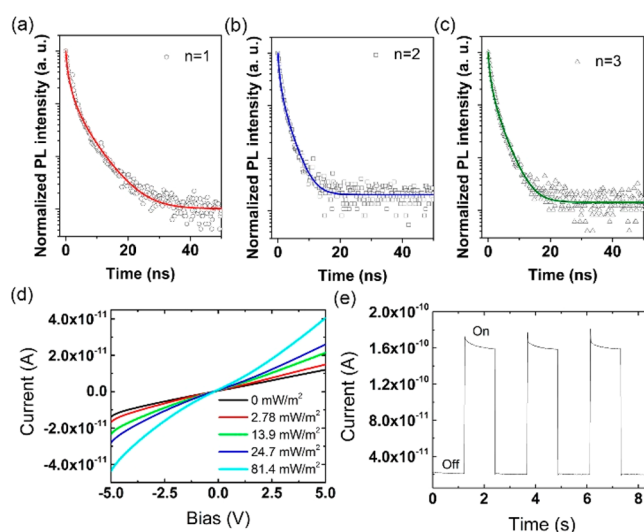

Figure 4. Time-resolved photoluminescence spectra of (a) $n = 1$ (β-Me-PEA)$_2$PbI$_4$, (b) $n = 2$ (β-Me-PEA)$_2$MAPb$_2$I$_7$, and (c) $n = 3$ (β-Me-PEA)$_2$MA$_2$Pb$_3$I$_{10}$ melt-processed films. (d) Current−voltage (I−V) scans and (e) current−time profile of the $n = 3$ melt-processed film under dark and illuminated conditions.

position of the PL peak therefore serves as a direct test of the film phase purity.[41] In each of the single-step $n = 1$ and two-step $n = 2$ and 3 melt-processed films, only one PL peak is observed, positioned at 517, 568, and 622 nm, respectively, coinciding with peak positions from $n = 1$, 2, and 3 crystals of analogous layered lead iodide perovskites.[40] Overall, XRD, absorption, and PL results all serve as strong evidence that these melt-processed films are composed of the intended phase-pure layered perovskites, in contrast to the typical situation of a phase mixture of different n. The SEM images of the melt-processed films also show that the grain sizes range from ∼50 μm for $n = 1$ to ∼10 μm for $n = 2$ and 3 (Figures S6−S8). Interestingly, for the $n = 3$ film, some of the platelet-shaped grains orient vertically instead of horizontally, in agreement with the small (110) and (220) peaks observed in the XRD pattern (Figure 3e).

As a control experiment, we also annealed spin-coated films with $n = 2$ and 3 overall composition under the same conditions as the postanneal for melt-processed films. However, this treatment alone did not lead to phase-pure films of $n = 2$ and 3, as confirmed by the XRD patterns (Figure S9), especially for the $n = 3$ film, which clearly contains the $n = 2$ phase as majority. We hypothesize that the first melting step is advantageous because it yields the correct stoichiometry after some organic species loss during melting; also, it might lead to better mixing of different phases by fast solidification from rapid cooldown from the melt state. The second step postannealing at 150 °C can mobilize the ions to form a single phase.[42−44] Postannealing at lower temperature (e.g., 100 °C) is less effective as it does not convert the films to a pure phase

rate equation (eq 1) including monomolecular and bimolecular recombination processes, as shown in the Experimental Section, similar to the models in previous reports.[45−47] By solving the differential equation (eqs 2 and 3), the PL decay traces can be fitted and the rate constant k_1 and the combination rate constant $k_2 \times N_0$ can be extracted (Table S1). Because the excited-state populations in these layered perovskites ($n < 4$) are primarily exciton-like, we attribute these two transitions to single exciton recombination and exciton−exciton annihilation. The k_1 value is the smallest for the $n = 1$ sample (0.18 ns^{-1}) and larger for the $n = 2$ and 3 samples (0.38 and 0.33 ns^{-1}, respectively). Compared with the values obtained from transient reflection measurements on single crystals,[47] the k_1 values are of the same order of magnitude. The combined rate constant $k_2 \times N_0$ does not show an obvious difference for different samples, but the exact value of the rate constant k_2 cannot be extracted accurately within the current experiment. A more detailed study of the photophysical properties of these two-step melt-processed films is currently underway.

Because the $n = 3$ film has the smallest band gap among the systems examined, it is perhaps the most relevant for optoelectronic applications such as photodetectors or photovoltaics. We therefore performed transport measurements using the two-step melt-processed films. Two-point current−voltage (I−V) scans were taken on films of different channel widths and lengths. The I−V curves of devices with various lengths/widths all show linear behavior, and the resistivity values extracted show relatively small variation with channel geometry (Figure S10), yielding 370 ± 50 Ω·m. The resistivity

values measured on single crystals of layered perovskites and MAPbI$_3$ range from ~10^5 to 10^6 Ω·m (i.e., several orders of magnitude higher values).[39,40] One of the reasons for this discrepancy is possibly "self-doping"[48−50] due to slight iodine or organic loss/deficiency from the thermal treatment. It is also worth noting that the current from the melt-processed films is ~10^{-6} A at 5 V, which is 2−3 orders of magnitude higher than for the spin-coated films (which contain a phase mixture of different n) (Figure S11). Such an increase presumably is due to improved crystallinity, grain size, orientation, and the "self-doping" effect. Interestingly, the conventional spin-coated films of $n = 3$ composition, although not phase pure, also show drastically increased conductivity after the same postannealing step (Figure S12). Similarly, for a $n = 1$ spin-coated film, a quick postanneal treatment also leads to ~2 orders of magnitude increase in conductivity (Figure S13). This observation suggests that such increase may be general for perovskites that undergo this thermal treatment. A more detailed study focused on the origin of the annealing-induced conductivity enhancement is currently underway and beyond the scope of this study.

The $n = 3$ film photoresponse was also evaluated by taking $I−V$ scans under dark and illumination conditions (using a white LED light source). The photocurrent increases with increasing light intensity as expected (Figure 4d) and exhibits good response to light on/off switching (Figure 4e). Because of the weak illumination intensity (1/5000 of 1 sun) the photocurrent density observed is in the range $10^{-2}−10^{-3}$ mA/cm^2, with an estimated responsivity of 0.4 A/W, which is within the range of the previously reported values for perovskite films and crystals.[40,51]

CONCLUSION

In conclusion, to move beyond our understanding of the $n = 1$ layered perovskites, we have synthesized and studied the thermal properties of $n = 2$ and 3 systems. Unlike the $n = 1$ compounds, higher n layered perovskites do not melt congruently, but rather undergo phase segregation into lower n and the 3D (MAPbI$_3$) compounds at the peritectic point. Nevertheless, melt-processing of these higher n perovskites can still be achieved, and with the addition of a postannealing step, highly crystalline and phase pure films have been demonstrated. The phase pure films have been further characterized by time-resolved photoluminescence measurements and electrical transport measurements. The melt-processed films show similar order of magnitude single-exciton recombination rate compared to previous reports and far higher conductivity compared to traditional spin-coated films. These results provide an ideal pathway to study these higher n materials and to develop an understanding of their intrinsic properties, which in turn can aid their implementation into high-performance optoelectronic devices.

ASSOCIATED CONTENT

ⓢ Supporting Information

The Supporting Information is available free of charge on the ACS Publications website at DOI: 10.1021/acs.chemmater.9b01265.

XRD profile fit, SEM images, TRPL fitting parameters, XRD, and $I−V$ scans of spin-coated and melt-processed films (PDF)

AUTHOR INFORMATION

Corresponding Author

*E-mail: david.mitzi@duke.edu.

ORCID ⓞ

Oana D. Jurchescu: 0000-0003-2204-2909

David B. Mitzi: 0000-0001-5189-4612

Notes

The authors declare no competing financial interest.

REFERENCES

(1) Mitzi, D. B. Synthesis, structure, and properties of organic-inorganic perovskites and related materials. In *Progress in Inorganic Chemistry*; Karlin, K. D., Ed.; John Wiley & Sons, Inc.: New York, 1999; Vol. 48, pp 1−121.

(2) Kojima, A.; Teshima, K.; Shirai, Y.; Miyasaka, T. Organometal Halide Perovskites as Visible-Light Sensitizers for Photovoltaic Cells. *J. Am. Chem. Soc.* **2009**, *131*, 6050−6051.

(3) Lee, M. M.; Teuscher, J.; Miyasaka, T.; Murakami, T. N.; Snaith, H. J. Efficient Hybrid Solar Cells Based on Meso-Superstructured Organometal Halide Perovskites. *Science* **2012**, *338*, 643−647.

(4) Burschka, J.; Pellet, N.; Moon, S.-J; Humphry-Baker, R.; Gao, P.; Nazeeruddin, M. K.; Gratzel, M. Sequential Deposition As A Route to High-Performance Perovskite-Sensitized Solar Cells. *Nature* **2013**, *499*, 316−319.

(5) Stranks, S. D.; Eperon, G. E.; Grancini, G.; Menelaou, C.; Alcocer, M. J. P; Leijtens, T.; Herz, L. M.; Petrozza, A.; Snaith, H. J. Electron-Hole Diffusion Lengths Exceeding 1 Micrometer in an Organometal Trihalide Perovskite Absorber. *Science* **2013**, *342*, 341−344.

(6) Tan, Z.-K.; Moghaddam, R. S.; Lai, M. L.; Docampo, P.; Higler, R.; Deschler, F.; Price, M.; Sadhanala, A.; Pazos, L. M.; Credgington, D.; et al. Bright Light-Emitting Diodes Based on Organometal Halide Perovskite. *Nat. Nanotechnol.* **2014**, *9*, 687−692.

(7) Dong, Q.; Fang, Y.; Shao, Y.; Mulligan, P.; Qiu, J.; Cao, L.; Huang, J. Electron-Hole Diffusion Lengths > 175 mm in Solution-grown CH$_3$NH$_3$PbI$_3$ Single Crystals. *Science* **2015**, *347*, 967−970.

(8) Byun, J.; Cho, H.; Wolf, C.; Jang, M.; Sadhanala, A.; Friend, R. H.; Yang, H.; Lee, T.-W. Efficient Visible Quasi-2D Perovskite Light-Emitting Diodes. *Adv. Mater.* **2016**, *28*, 7515−7520.

(9) Wang, N.; Cheng, L.; Ge, R.; Zhang, S.; Miao, Y.; Zou, W.; Yi, C.; Sun, Y.; Cao, Y.; Yang, R.; et al. Perovskite Light-Emitting Diodes Based on Solution-processed Self-Organized Multiple Quantum Wells. *Nat. Photonics* **2016**, *10*, 699−704.

(10) Yuan, M.; Quan, L. N.; Comin, R.; Walters, G.; Sabatini, R.; Voznyy, O.; Hoogland, S.; Zhao, Y.; Beauregard, E. M.; Kanjanaboos, P.; et al. Perovskite Energy Funnels for Efficient Light-emitting Diodes. *Nat. Nanotechnol.* **2016**, *11*, 872−877.

(11) Lin, K.; Xing, J.; Quan, L. N.; de Arquer, F. P. G; Gong, X.; Lu, J.; Xie, L.; Zhao, W.; Zhang, D.; Yan, C.; et al. Perovskite light-emitting diodes with external quantum efficiency exceeding 20%. *Nature* **2018**, *562*, 245–248.

(12) Zhao, B.; Bai, S.; Kim, V.; Lamboll, R.; Shivanna, R.; Auras, F.; Richter, J. M.; Yang, L.; Dai, L.; Alsari, M.; et al. High-efficiency perovskite–polymer bulk heterostructure light-emitting diodes. *Nat. Photonics* **2018**, *12*, 783–789.

(13) Stoumpos, C. C.; Cao, D. H.; Clark, D. J.; Young, J.; Rondinelli, J. M.; Jang, J. I.; Hupp, J. T.; Kanatzidis, M. G. Ruddlesden–Popper Hybrid Lead Iodide Perovskite 2D Homologous Semiconductors. *Chem. Mater.* **2016**, *28*, 2852–2867.

(14) Calabrese, J.; Jones, N. L.; Harlow, R. L.; Herron, N.; Thorn, D. L.; Wang, Y. Preparation and characterization of layered lead halide compounds. *J. Am. Chem. Soc.* **1991**, *113*, 2328–2330.

(15) Mitzi, D. B.; Feild, C. A.; Harrison, W. T. A; Guloy, A. M. Conducting tin halides with a layered organic-based perovskite structure. *Nature* **1994**, *369*, 467–469.

(16) Smith, I. C.; Hoke, E. T.; Solis-Ibarra, D.; McGehee, M. D.; Karunadasa, H. I. A Layered Hybrid Perovskite Solar-Cell Absorber with Enhanced Moisture Stability. *Angew. Chem., Int. Ed.* **2014**, *53*, 11232–11235.

(17) Cao, D. H.; Stoumpos, C. C.; Farha, O. K.; Hupp, J. T.; Kanatzidis, M. G. 2D Homologous Perovskites as Light-Absorbing Materials for Solar Cell Applications. *J. Am. Chem. Soc.* **2015**, *137*, 7843–7850.

(18) Tsai, H.; Nie, W.; Blancon, J.-C; Stoumpos, C. C.; Asadpour, R.; Harutyunyan, B.; Neukirch, A. J.; Verduzco, R.; Crochet, J. J.; Tretiak, S.; et al. High-Efficiency Two-Dimensional Ruddlesden–Popper Perovskite Solar Cells. *Nature* **2016**, *536*, 312–316.

(19) Wang, N.; Cheng, L.; Ge, R.; Zhang, S.; Miao, Y.; Zou, W.; Yi, C.; Sun, Y.; Cao, Y.; Yang, R.; et al. Perovskite light-emitting diodes based on solution-processed self-organized multiple quantum wells. *Nat. Photonics* **2016**, *10*, 699–704.

(20) Mao, L.; Stoumpos, C. C.; Kanatzidis, M. G. Two-Dimensional Hybrid Halide Perovskites: Principles and Promises. *J. Am. Chem. Soc.* **2019**, *141*, 1171–1190.

(21) Sharenko, A.; Toney, M. F. Relationships Between Lead Halide Perovskite Thin-Film Fabrication, Morphology, and Performance In Solar Cells. *J. Am. Chem. Soc.* **2016**, *138*, 463–470.

(22) Seo, J.; Noh, J. H.; Seok, S. I. Rational Strategies for Efficient Perovskite Solar Cells. *Acc. Chem. Res.* **2016**, *49*, 562–572.

(23) Zhou, Y.; Yang, M.; Wu, W.; Vasiliev, A. L.; Zhu, K.; Padture, N. P. Room-temperature crystallization of hybrid-perovskite thin films via solvent–solvent extraction for high-performance solar cells. *J. Mater. Chem. A* **2015**, *3*, 8178–8184.

(24) Yang, M.; Zhou, Y.; Zeng, Y.; Jiang, C.-S; Padture, N. P.; Zhu, K. Square-Centimeter Solution-Processed Planar $CH_3NH_3PbI_3$ Perovskite Solar Cells with Efficiency Exceeding 15%. *Adv. Mater.* **2015**, *27*, 6363–6370.

(25) Saliba, M.; Correa-Baena, J.-P; Wolff, C. M.; Stolterfoht, M.; Phung, N.; Albrecht, S.; Neher, D.; Abate, A. How to Make over 20% Efficient Perovskite Solar Cells in Regular (n–i–p) and Inverted (p–i–n) Architectures. *Chem. Mater.* **2018**, *30*, 4193–4201.

(26) Zeidell, A. M.; Tyznik, C.; Jennings, L.; Zhang, C.; Lee, H.; Guthold, M.; Vardeny, Z. V.; Jurchescu, O. D. Enhanced Charge Transport in Hybrid Perovskite Field-Effect Transistors via Microstructure Control. *Adv. Electron. Mater.* **2018**, *4*, 1800316.

(27) Stoumpos, C. C.; Soe, C. M. M; Tsai, H.; Nie, W.; Blancon, J.-C; Cao, D. H.; Liu, F.; Traoré, B.; Katan, C.; Even, J.; et al. High Members of the 2D Ruddlesden-Popper Halide Perovskites: Synthesis, Optical Properties, and Solar Cells of $(CH_3(CH_2)_3NH_3)_2(CH_3NH_3)_4Pb_5I_{16}$. *Chem. Mater.* **2017**, *2*, 427–440.

(28) Zhou, N.; Shen, Y.; Li, L.; Tan, S.; Liu, N.; Zheng, G.; Chen, Q.; Zhou, H. Exploration of Crystallization Kinetics in Quasi Two-Dimensional Perovskite and High Performance Solar Cells. *J. Am. Chem. Soc.* **2018**, *140*, 459–465.

(29) Mitzi, D. B.; Dimitrakopoulos, C. D.; Rosner, J.; Medeiros, D. R.; Xu, Z.; Noyan, C. Hybrid Field-Effect Transistor Based on a Low-Temperature Melt-Processed Channel Layer. *Adv. Mater.* **2002**, *14*, 1772–1776.

(30) Mitzi, D. B.; Medeiros, D. R.; DeHaven, P. W. Low-Temperature Melt Processing of Organic-Inorganic Hybrid Films. *Chem. Mater.* **2002**, *14*, 2839–2841.

(31) Papavassiliou, G. C.; Koutselas, I. B.; Mousdis, G. A.; Papaioannou, G. J. Some Organic-Inorganic Hybrid Semiconductors Obtained from Melts. In *Molecular Low Dimensional and Nanostructured Materials for Advanced Applications*; Graja, A., Bułka, B. R.; Kajzar, F., Eds.; Springer Netherlands: Dordrecht, 2002; Vol. *59*, pp 319–322.

(32) Papavassiliou, G. C.; Mousdis, G. A.; Anyfantis, G. C. Organic-Inorganic Hybrid Compounds Based on Lead Halide Units: Preparation from Melts and through Grinding Effects. *Z. Naturforsch., B: J. Chem. Sci.* **2010**, *65*, 516–520.

(33) Papavassiliou, G. C.; Koutselas, J. B.; Lagouvardos, D. J. Preparation and Characterization of $(C_6H_5CH_2CH_2NH_3)_2SnI_4$ and $(C_6H_5CH_2CH_2NH_3)_2SnBr_4$. *Z. Naturforsch, B: J. Chem. Sci.* **1993**, *48*, 1013–1014.

(34) Rabolt, J. F.; Clarke, T. C.; Kanazawa, K. K.; Reynolds, J. R.; Street, G. B. Organic Metals: Poly-(p-phenylene sulphide) Hexafluoroarsenate. *J. Chem. Soc., Chem. Commun.* **1980**, *0*, 347–348.

(35) Holesinger, T. G.; Phillips, D. S.; Coulter, J. Y.; Willis, J. O.; Peterson, D. E. Isothermal melt processing of Bi-2212 thick films. *Phys. C* **1995**, *243*, 93–102.

(36) Wideman, T.; Sneddon, L. G. Dipentylamine-Modified Polyborazylene: A New, Melt-Spinnable Polymeric Precursor to Boron Nitride Ceramic Fibers. *Chem. Mater.* **1996**, *8*, 3–5.

(37) Li, T.; Dunlap-Shohl, W. A.; Han, Q.; Mitzi, D. B. Melt Processing of Hybrid Organic–Inorganic Lead Iodide Layered Perovskites. *Chem. Mater.* **2017**, *29*, 6200–6204.

(38) Li, T.; Dunlap-Shohl, W. A.; Reinheimer, E. W.; Le Magueres, P.; Mitzi, D. B. Melting temperature suppression of layered hybrid lead halide perovskites via organic ammonium cation branching. *Chem. Sci.* **2019**, *10*, 1168–1175.

(39) Stoumpos, C. C.; Malliakas, C. D.; Kanatzidis, M. G. Semiconducting Tin and Lead Iodide Perovskites with Organic Cations: Phase Transitions, High Mobilities, and Near-Infrared Photoluminescent Properties. *Inorg. Chem.* **2013**, *52*, 9019–9038.

(40) Peng, W.; Yin, J.; Ho, K.-T; Ouellette, O.; De Bastiani, M.; Murali, B.; El Tall, O.; Shen, C.; Miao, X.; Pan, J.; et al. Ultralow Self-Doping in Two-dimensional Hybrid Perovskite Single Crystals. *Nano Lett.* **2017**, *17*, 4759–4767.

(41) Hu, Y.; Spies, L. M.; Alonso-Álvarez, D.; Mocherla, P.; Jones, H.; Hanisch, J.; Bein, T.; Barnes, P. R. F; Docampo, P. Identifying and controlling phase purity in 2D hybrid perovskite thin films. *J. Mater. Chem. A* **2018**, *6*, 22215–22225.

(42) Yang, T.-Y; Gregori, G.; Pellet, N.; Grätzel, M.; Maier, J. The Significance of Ion Conduction in a Hybrid Organic–Inorganic Lead-Iodide-Based Perovskite Photosensitizer. *Angew. Chem., Int. Ed.* **2015**, *54*, 7905–7910.

(43) Xing, J.; Wang, Q.; Dong, Q.; Yuan, Y.; Fang, Y.; Huang, J. Ultrafast ion migration in hybrid perovskite polycrystalline thin films under light and suppression in single crystals. *Phys. Chem. Chem. Phys.* **2016**, *18*, 30484–30490.

(44) Eames, C.; Frost, J. M.; Barnes, P. R. F; O'Regan, B. C.; Walsh, A.; Islam, M. S. Ionic transport in hybrid lead iodide perovskite solar cells. *Nat. Commun.* **2015**, *6*, 7497.

(45) Dastidar, S.; Li, S.; Smolin, S. Y.; Baxter, J. B.; Fafarman, A. T. Slow Electron–Hole Recombination in Lead Iodide Perovskites Does Not Require a Molecular Dipole. *ACS Energy Lett.* **2017**, *2*, 2239–2244.

(46) Yang, Y.; Yang, M.; Li, Z.; Crisp, R.; Zhu, K.; Beard, M. C. Comparison of Recombination Dynamics in $CH_3NH_3PbBr_3$ and $CH_3NH_3PbI_3$ Perovskite Films: Influence of Exciton Binding Energy. *J. Phys. Chem. Lett.* **2015**, *6*, 4688–4692.

(47) Chen, X.; Lu, H.; Li, Z.; Zhai, Y.; Ndione, P. F.; Berry, J. J.; Zhu, K.; Yang, Y.; Beard, M. C. Impact of Layer Thickness on the Charge Carrier and Spin Coherence Lifetime in Two-Dimensional

Layered Perovskite Single Crystals. *ACS Energy Lett.* **2018**, 3, 2273−2279.

(48) Xie, H.; Liu, X.; Lyu, L.; Niu, D.; Wang, Q.; Huang, J.; Gao, Y. Effects of Precursor Ratios and Annealing on Electronic Structure and Surface Composition of $CH_3NH_3PbI_3$ Perovskite Films. *J. Phys. Chem. C* **2016**, *120*, 215−220.

(49) Wang, Q.; Shao, Y.; Xie, H.; Lyu, L.; Liu, X.; Gao, Y.; Huang, J. Qualifying composition dependent p and n self-doping in $CH_3NH_3PbI_3$. *Appl. Phys. Lett.* **2014**, *105*, 163508.

(50) Paul, G.; Chatterjee, S.; Bhunia, H.; Pal, A. J. Self-Doping in Hybrid Halide Perovskites via Precursor Stoichiometry: To Probe the Type of Conductivity through Scanning Tunneling Spectroscopy. *J. Phys. Chem. C* **2018**, *122*, 20194−20199.

(51) Ahmadi, M.; Wu, T.; Hu, B. A Review on Organic−Inorganic Halide Perovskite Photodetectors: Device Engineering and Fundamental Physics. *Adv. Mater.* **2017**, *29*, 1605242−1605265.